PUBLICATION V

NBI torque in the presence of magnetic field ripple: experiments and modelling for JET

In: Plasma Physics and Controlled Fusion 53,
085005 (20 pp), 2011.

http://iopscience.iop.org/0741-3335/53/8/085005/
pdf/0741-3335_53_8_085005.pdf

Plasma Phys. Control. Fusion **53** (2011) 085005 (20pp) doi:10.1088/0741-3335/53/8/085005

NBI torque in the presence of magnetic field ripple: experiments and modelling for JET

A T Salmi[1], T Tala[2], G Corrigan[3], C Giroud[3], J Ferreira[4], J Lönnroth[1], P Mantica[5], V Parail[3], M Tsalas[6], T W Versloot[6], P C de Vries[6], K-D Zastrow[3] and EFDA JET Contributors[7]

JET-EFDA, Culham Science Centre, Abingdon, OX14 3DB, UK
[1] Aalto University, Association Euratom-Tekes, Helsinki, Finland
[2] VTT, Association Euratom-Tekes, Helsinki, Finland
[3] EURATOM/CCFE Fusion Association, Culham Science Centre, Abingdon, UK
[4] Associação EURATOM/IST, Centro de Fusão Nuclear, 1049-001 Lisbon, Portugal
[5] Istituto di Fisica del Plasma, Euratom-ENEA-CNR Association, Milan, Italy
[6] FOM Institute Rijnhuizen, Association EURATOM-FOM, Nieuwegein, the Netherlands

Received 5 January 2011, in final form 30 March 2011
Published 19 May 2011
Online at stacks.iop.org/PPCF/53/085005

Abstract
Accurate and validated tools for calculating toroidal momentum sources are necessary to make reliable predictions of toroidal rotation for current and future experiments. In this work we present the first experimental validation of torque profile calculation from neutral beam injection (NBI) under toroidal field ripple. We use discharges from a dedicated experimental session on JET where neutral beam modulation technique is used together with time-dependent torque calculations from ASCOT code for making the benchmark. Good agreement between simulations and experimental results is found.

(Some figures in this article are in colour only in the electronic version)

1. Introduction

Toroidal momentum transport and rotation have been very active research topics in the last years. Toroidal rotation and rotation shear have been shown to improve confinement [1] and to increase the stability against resistive wall modes [2] of fusion plasmas. Recently it has been shown, both theoretically [3, 4] and experimentally [5–8], that inside the plasma pedestal, momentum transport is not purely diffusive but that a convective (pinch) term also exists. Inward momentum pinch may help to achieve a peaked rotation profile in ITER, even with just small external torque sources or with other seed rotation sources at the plasma edge [9].

[7] See the appendix of Romanelli F *et al* 2010 *Proc. 23rd IAEA Fusion Energy Conf. 2010 (Daejon, Korea)*.

One important ingredient in predicting rotation in ITER is the capability to calculate the torque generated by the neutral beam injection (NBI) under toroidal magnetic field ripple. Even with the ripple compensating ferromagnetic inserts included in the design, the expected ripple magnitude $\delta = (B_{\max} - B_{\min})/(B_{\max} + B_{\min})$ in the full field will be $\delta \sim 0.35\%$, which although shown to be acceptable in terms of fast ion energy losses [10], may still cause a significant counter-current torque contribution via non-ambipolar radial diffusion of fast ions. In recent JET experiments [11] with enhanced ripple ($\delta \sim 1\%$), the plasma edge was found to counter-rotate with co-current NBI while similar plasmas with smaller ripple were co-rotating. It was found that, taking into account the NBI torque modification due to the ripple, the observations could be largely explained. In rippled Ohmic plasmas in JET, counter-current torque contribution due to ripple has also been observed, although the level of rotation has been small compared with NBI heated discharges [12].

Non-axisymmetric magnetic perturbations, such as toroidal field ripple, can lead to non-ambipolar radial transport of not only fast ions but also of thermal ions giving rise to the so-called neoclassical toroidal viscosity (NTV) torque, see, e.g., a recent review [13] and references therein. Plasma breaking, associated with NTV, has indeed been observed experimentally on several tokamaks, e.g. DIII-D and JET using low toroidal harmonic magnetic perturbations. Toroidal field ripple, on the other hand, has a weak radial component, which decays rapidly towards the plasma centre. The associated NTV torque, whether small or large, is expected to be edge localized. It is assumed that in the discharges analysed here NBI is the dominant *core* torque source and other possible torque sources such as the NTV or the residual stress [14] are neglected.

While ripple diffusion and trapping are well understood theoretically and experimentally [15–19], the rigorous validation of fast ion ripple torque calculations against experimental data is still lacking. Numerous earlier studies on ripple losses [20, 21], fast ion neutron yield [22, 23] and prompt momentum balance [24] already indirectly suggest that guiding centre following codes should be capable of this task also with ripple. In previous works from the JET ripple campaign [11, 25], the ripple induced fast ion losses and torque have, indeed, been identified as the likely candidate to explain the observed reduction in rotation. However, without detailed knowledge of the momentum transport in the discharges, only rough estimates of the total torque can be obtained. For validating the torque calculations in the presence of ripple, dedicated experiments are required in which both the diffusive and convective momentum transport (χ_ϕ and v_{pinch}) and the effect of ripple on NBI torque can be resolved simultaneously.

In this work, discharges from the JET enhanced ripple session designed for benchmarking the NBI torque calculations in the presence of toroidal field ripple are analysed. The guiding centre following Monte Carlo code ASCOT [26] is used for the torque calculations. ASCOT has been used for fast ion loss calculations with ripple in, e.g., [27, 28] but has not yet been experimentally validated for the torque.

The rest of the paper is organized as follows. First, the experimental set-up is described and a justification for the assumption of an identical and stationary momentum transport between the discharges is given. This is followed by a description of the plasma response to the applied NBI torque and power modulation. Section 3 is dedicated for code-to-code benchmarking. ASCOT is first briefly described, after which the comparisons against OFMC [19, 29] and NUBEAM (inside the TRANSP transport code) [30] are presented. In Section 4, the time-dependent NBI torque profiles from ASCOT are reviewed, and compared against the experimental rotation data in Fourier space at the modulation frequency. Section 5 describes the optimization scheme used to evaluate the momentum transport coefficients, and presents the comparison between the simulated toroidal rotation, using torque from ASCOT, and the experimental data. Finally, the results are discussed and conclusions of the work are drawn in section 6.

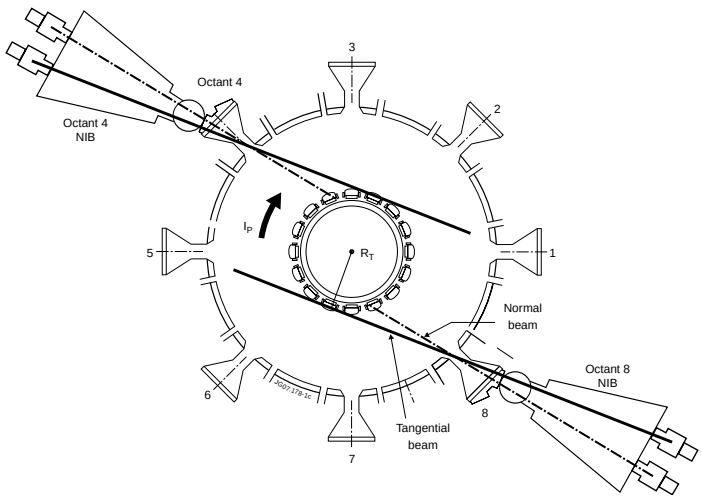

Figure 1. Top view of the JET NBI system. The toroidal field is in the same direction as the current.

2. Experimental set-up

The NBI system at JET [31] consists of a total of 16 units each capable of delivering roughly 1–1.5 MW of power and 1–1.5 Nm of torque depending on the voltage and injection angle used. Half of the units are aligned with a tangency radius of $R_{\mathrm{T}} = 1.31$ m (normal injection) while the rest have a tangency radius of $R_{\mathrm{T}} = 1.85$ m (tangential injection) in the usual co-current direction, see figure 1. The major radius of the JET torus is $R_0 = 2.95$ m. NBI acceleration voltages can be adjusted in the range 60–130 kV as required by the experiment. NBI power can also be turned on and off relatively reliably thus lending itself to transport studies utilizing modulation techniques [32, 33].

A set of discharges was selected for this study (77089, 77090 and 77091), characterized by L-mode confinement and hence a relatively low density ($n_{\mathrm{e0}} \approx 3 \times 10^{19}\,\mathrm{m}^{-3}$) and low temperature ($T_{\mathrm{e0}} \approx T_{\mathrm{i0}} \approx 3$ keV), and all with a plasma current of $I_{\mathrm{p}} = 1.5$ MA and the average central toroidal field $B_0 = 2.2$ T ($q_{95} = 5$). The three discharges did not exhibit MHD activity. In each discharge two 90 keV NBI units (total of 2.5 MW) are injected continuously to collect ion temperature and toroidal rotation data and to keep that plasma relatively stationary during the experimental window. Additionally, two/three modulated 65 keV units (≈4.5 MW) are used with a duty cycle of 50/110 ms (on/off). The modulation cycle is short enough to avoid reaching steady state yet long enough to yield plasma rotation modulation sufficiently large to make the analysis. Discharge 77089 is the reference without ripple and with normal NBI modulation (3 units). 77090 is identical to 77089 but operated with 1.5% toroidal field ripple. 77091 is again a similar discharge with ripple, but with modulation from tangential NBI units (2 units).

Figure 2 shows time traces of a number of important plasma and heating parameters for the reference discharge 77089 with small ripple ($\delta = 0.08\%$). The time interval is the same which is used for transport and torque analysis as well as for the Fourier analysis of the experimental

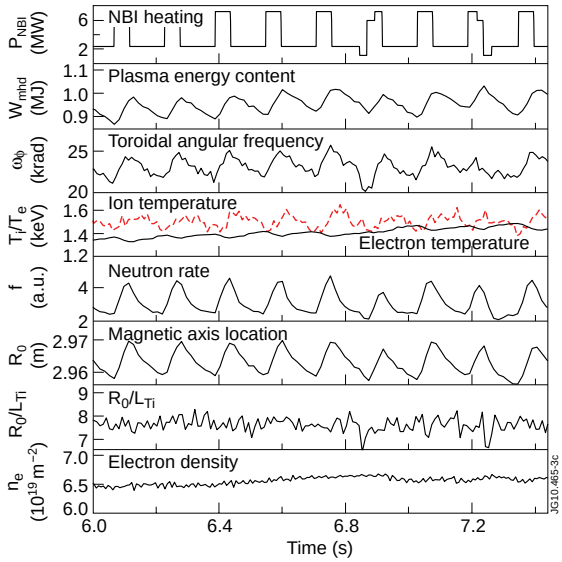

Figure 2. Time traces of plasma and heating parameters over the time interval of interest for 77089. Temperature and rotation values are taken near plasma midradius and magnetic axis from EFIT [35] reconstruction.

profiles. One can observe that all the chosen quantities are modulated with the NBI, except the electron density and the normalized inverse temperature scale length, $R_0/L_{T_\mathrm{i}} = R_0\nabla T_\mathrm{i}/T_\mathrm{i}$. The highest fractional increase is seen in the total neutron rate which is dominated by the beam thermal D–D fusion. Other quantities are dominated by the changes in the bulk plasma and therefore fluctuate significantly less. A more detailed investigation across the radius shows that the ion and electron temperature modulations remain at a moderate 2–5% level, while the toroidal rotation fluctuation can reach levels up to 10%.

In general, the radial momentum transport is proportional to heat transport [34]. In these low performance L-mode plasmas the main driver of the momentum transport is the ITG turbulence. As seen in figure 2, the electron density stays constant and does not modulate with the NBI (negligible fuelling effect). Furthermore, the small ion temperature fluctuation is compensated by the accompanying ∇T_i fluctuation, and the temperature scale length, L_{T_i}, is practically uncorrelated with the modulation. These give a good indication that the local momentum transport stays independent of the NBI modulation throughout the experiment. Therefore, we can simplify the subsequent analysis by assuming constant transport (in time) and keep the momentum transport coefficients fixed during the time interval of interest.

This approximation is also supported by the previous work [33, section IV.A2], where the effect of the fluctuating energy diffusion χ_i due to T_i oscillations was studied. It was found that for small T_i amplitudes the rotation response of the plasma did not change significantly when the fluctuations in χ_i were included in the analysis.

The similarity of the plasmas across the discharges is seen in figure 3, where the experimental steady-state profiles are plotted for the discharges 77089–77091. Ion and electron temperature profiles as well as the q-profiles are practically the same for all the plasmas and the

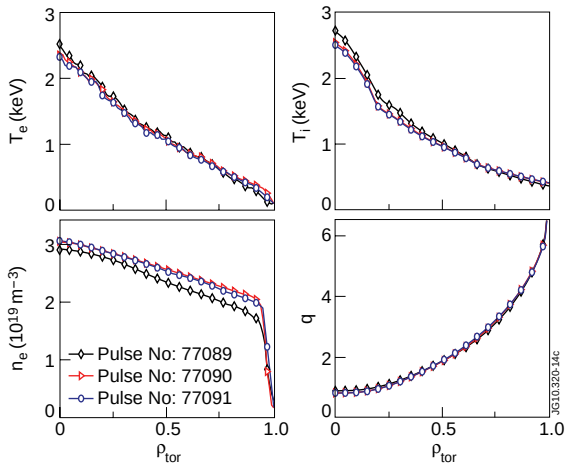

Figure 3. Time averaged plasma and q-profiles over 9 modulation cycles between 46.0–47.44 s for the discharges 77089 (diamond), 77090 (triangle) and between 47.0–48.44 s for 77091 (circle).

difference in electron density between the high ripple discharges and the reference discharge is below 10%. Based on the similar profiles among the three discharges we assume that the transport of momentum is the same between them, and that the difference in the rotation is due to the difference in the torque source. More precisely, we assume that the Prandtl number, $Pr = \chi_\phi/\chi_\mathrm{i}$, and the pinch velocity, v_pinch, are equal between the discharges. This should be a reasonable assumption for the Prandtl number since the variation in electron density should affect the χ_ϕ and χ_i in the same way. To estimate the sensitivity of the v_pinch on the density we can use the experimental scaling, $Rv_\mathrm{pinch}/\chi_\phi \approx 1.2R/L_n + 1.4$ [9]. Dividing the formula by parts and substituting experimental values we find that for $\rho_\mathrm{tor} < 0.8$ the ratio $v_\mathrm{pinch,77089}/v_\mathrm{pinch,77090}$ is between 0.9 and 1.1. The experimental estimate of the pinch velocity sensitivity is less than the error we get in the transport analysis.

In addition to the plasma properties, the location of the magnetic axis is modulated due to the NBI driven change in the plasma pressure. In fact the whole plasma moves almost rigidly. During the high power phase the magnetic axis moves about 1 cm, and the separatrix 8 mm, towards the low-field side. The equilibrium modulation combined with radial gradients in the profiles can generate spurious components in signals which are collected along fixed lines of sight. A simple estimation, using the 5 mm radial modulation and the gradients involved, shows that this could contribute about 5–20% to the modulation amplitudes if not subtracted in an appropriate way. In the following we eliminate this effect by mapping the data into time-independent flux surface coordinates prior to the analyses.

A further complication coming from the equilibrium modulation is the change in the ripple magnitude at a given flux surface (see figure 4). The radial decay length of the ripple magnitude at separatrix is about $\lambda_\mathrm{r} = 25$ cm which for the 8 mm displacement results in a 3% change in the effective ripple magnitude. To quantify how big a difference it makes on the torque, we have run ASCOT at both extremities to find that the counter-current torque is increased by ∼3% when the ripple is larger. Due to the smallness of this effect we neglect it and for simplicity fix the equilibrium for the whole analysis period.

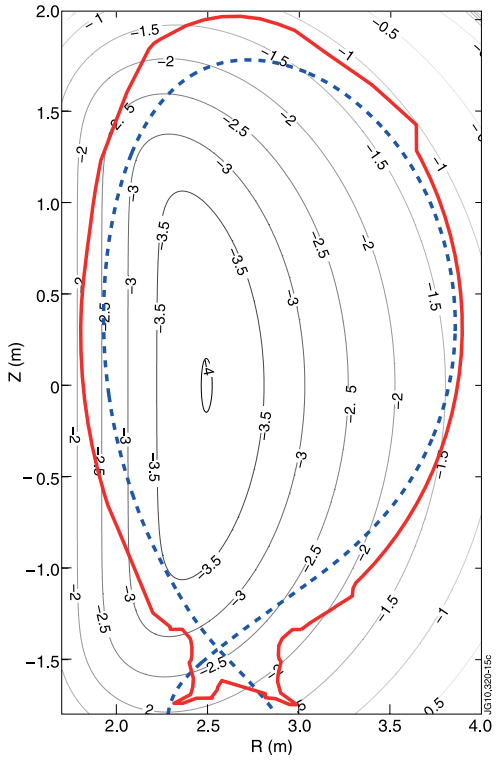

Figure 4. Ripple map for JET 16 coil harmonic together with the cross section of the limiter surface and a separatrix for a typical equilibrium. Numbers on the contours give the $\log_{10}$ of the ripple amplitude.

3. Code-to-code benchmarking

Multiple studies have been conducted regarding the ripple effects, e.g. [15, 16, 36], producing analytical formulae and insights into the physical mechanisms. However, the analytical approach is difficult for realistic simulations when complicating factors arise, e.g. from the geometry of the toroidal field coils, plasma shape, NBI geometry or from the asymmetry of the fast ion distributions. These effects are, however, straightforward to include in the orbit following Monte Carlo codes, as are Coulomb collisions and their synergy with ripple. Nevertheless, it is useful, and helps to interpret the results later on, to see what parameters are involved in ripple banana diffusion [15]

$$\Delta = (N\pi/\sin\theta_t)^{1/2}\left(\frac{q}{\epsilon}\right)^{3/2}\rho\delta\cdot\cos N\phi_t. \tag{1}$$

Here Δ is the radial step size in ripple diffusion at the banana tip, N is the number of toroidal field coils, θ_t and ϕ_t are the poloidal and toroidal angles of the turning point, q is the safety factor, ϵ the inverse of the aspect ratio, ρ the gyro-radius of the ion and δ the ripple

amplitude $\delta = (B_{\max} - B_{\min})/(B_{\min} + B_{\max})$. Even though this formula has been derived for circular plasmas with circular coils it shows that, since the diffusion coefficient $D = \Delta^2\tau^{-1}$ (τ = bounce time), under similar plasma conditions the diffusion is stronger for ions with higher energy and smaller pitch angle (=smaller θ_t) and in areas where the ripple is larger.

3.1. The ripple model in ASCOT

Magnetic field ripple related phenomena from trapping to stochastic ripple diffusion are automatically included in the guiding centre orbit following codes when ions are traced in the full 3D magnetic field. For simulating JET plasmas with ASCOT we superimpose a sinusoidally varying toroidal magnetic field ripple on top of the axi-symmetric equilibrium field, B_0

$$B(r, z, \phi) = B_0(r, z)[1 + \delta_{16}(r, z)\cos 16\phi + \delta_{32}(r, z)\cos 32\phi].$$

Here, the axi-symmetric part is taken from EFIT. The numeric subscripts denote the $N = 16$ and $N = 32$ toroidal harmonic of the Fourier decomposed vacuum ripple map. The original 3D vacuum ripple field, from which the toroidal harmonics are extracted, is simply calculated using the Biot–Savart law by approximating the toroidal field coils with current filaments. In reality, the plasma response to the non-axisymmetric perturbation can generate currents that either screen or enhance the vacuum perturbations. Earlier studies with self-consistent 3D equilibrium codes [37, 38], however, have shown that the vacuum field approximation for the toroidal field ripple is adequate.

During the usual JET operation, all 32 toroidal field coils are driven with an equal amount of current. In this case the level of toroidal field ripple is very low, $\delta_{32} \approx 0.08\%$ at the outboard midplane near the separatrix. In the ripple configuration, the even and odd numbered toroidal field coils can be driven independently giving raise to the $N = 16$ harmonic ripple component. At elevated ripple it is the $N = 16$ harmonic ripple component that gives the dominant effect. This can readily be seen from equation (1). Namely, the diffusion coefficient, $D \propto \Delta^2 \propto N\delta^2$, shows that strongest diffusion comes from δ_{16} as soon as $\delta_{16} \gtrsim 0.12\%$. In these experiments $\delta_{16} \sim 1.5\%$. Figure 4 shows the ripple contours for the pure $N = 16$ harmonic. The toroidal field ripple is largest at the outboard side of the plasma, slightly above the midplane. Although significant near the edge, the ripple field decays rapidly towards the core of the plasma, and it becomes negligible inside the inner half of the plasma.

3.2. ASCOT *benchmark against* OFMC *and* TRANSP

In order to gain general trust in ASCOT calculations we compare it against two other well known codes, OFMC [10, 19, 29] and NUBEAM (inside the TRANSP transport code) [30]. OFMC has been developed and used extensively for JFT-2M and JT-60U and it has been successfully benchmarked against several experimental data [19–21, 39]. More recently OFMC has also been used for JET in preparation and analysis of JET ripple campaign, where good quantitative agreement between the OFMC calculated heat loads due to fast ion losses and experimental values determined by the infra red camera were found [40].

Figure 5 shows an example of ASCOT calculation of the heat load on limiters and on the first wall on the low-field side of the vacuum vessel during high ripple operation. The main heat load from NBI is deposited on the poloidal limiters (grey bars) near the equatorial plane. Heat load on limiters increases with ripple while at the same time localized heat loads below the midplane appear due to ripple trapping. This toroidally periodic heat load pattern, here around poloidal angle, $\theta \sim -70^\circ$, is due to the ripple trapped ions drifting vertically down from the high ripple region. The pattern and localization of these heat loads are well suited for a code-to-code comparison of ripple losses.

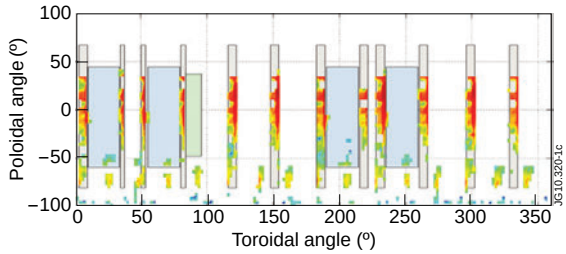

Figure 5. 2D projection of the heat load on the first wall and limiters from NBI in JET under 1.5% ripple as calculated by ASCOT. Blue rectangles show the RF and LH antennas and grey elongated structures the poloidal limiters designed to withstand heat loads up to several MW m^{-2}.

Both ASCOT and OFMC have been used extensively in the preparation and in the analysis of the JET ripple campaigns in 2006–2008 during which they have been cross checked against each other. Here we present one of the comparisons where both codes use a toroidally symmetric 2D limiter surface for clarity and statistics. Both codes use the EFIT equilibrium of the JET discharge 60856 together with the experimental temperature and density profiles. In this example we show data from simulations with artificially high ripple ($\delta \approx 3\%$) with 1 MW of 130 keV NBI. Both codes use their own model for the NBI geometry and for calculating the initial ionization (birth profile).

One can see in the left frame of figure 6 that the codes predict nearly identical heat load patterns with the maximum loads deviating less than 10%. The toroidal angles $\phi = 0^\circ$ and $\phi = 22.5^\circ$ correspond to the location of the high current coils, i.e. ripple minima and the dashed line at $\phi = 11.25^\circ$ correspond to the ripple well. Also, as expected, due to the $1/R$ dependence of the toroidal magnetic field, both codes show a slight shift of the maximum heat load from the ripple minimum in the co-current direction (here ϕ increases in counter-current direction). The right frame shows a comparison of the energy distribution of the ions that cause the heat load on the limiter surface. At higher energies the curves are nearly identical. The deviation at lower energies is due to different lower energy thresholds. Here ASCOT stops ion tracing at higher average energy which yields smaller losses at lower energies.

ASCOT torque calculations and its time-dependent operation without ripple have already been benchmarked against TRANSP in the earlier work [33] with good agreement. Comparisons were made for different discharges, separately for $\boldsymbol{j} \times \boldsymbol{B}$ and collisional torque components and at various beam modulation frequencies. Here, a further comparison between these codes using the reference discharge (77089) is presented. The calculated time-dependent torque profiles from both codes are Fourier transformed at the 6.25 Hz NBI modulation frequency and the resulting torque amplitude, phase and steady-state profiles are shown in figure 7. The reference phase is taken from the injected NBI power, i.e. zero phase corresponds to an instantaneous torque. Note that the phase and amplitude profiles are both related to the dynamics of the torque evaluation. The agreement between the codes is good, both in the magnitude, and in the shape of the profiles.

4. Experimental data analysis

4.1. Torque evaluation

For calculating the NBI torque we use the experimental NBI power waveforms, acceleration voltages and fractions for the E, $E/2$ and $E/3$ energy components. For simplicity, since the

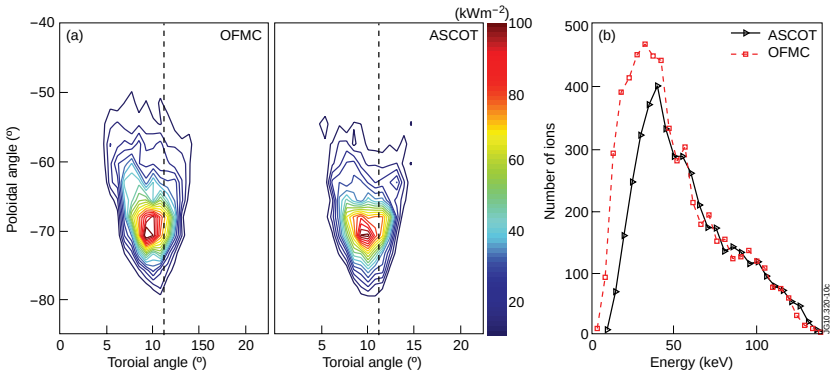

Figure 6. (*a*) Heat load from the ripple trapped ions in the ripple well region as calculated by OFMC and ASCOT. Dashed line shows the toroidal location of ripple minimum. (*b*) Energy spectra of the ripple trapped losses.

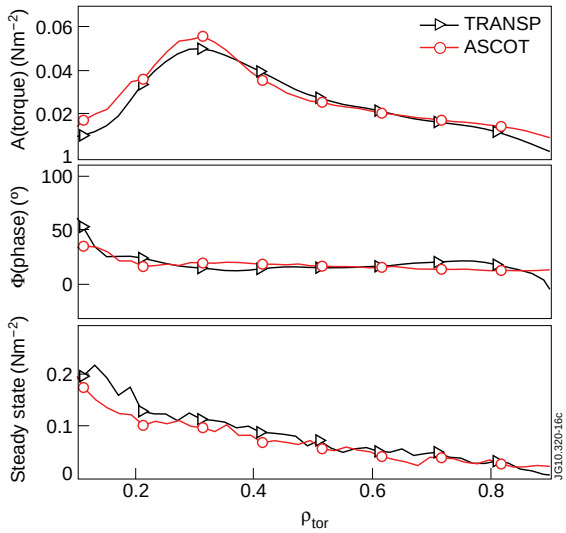

Figure 7. Comparison of ASCOT and TRANSP torque evaluation for the reference discharge (77089). Frames from the top show the Fourier amplitude profile at the 6.25 Hz modulation frequency, the Fourier phase with respect to the NBI power, and the steady-state torque transfer.

plasma profiles are not significantly modulated by the NBI, we time average all the profiles and keep them constant during beam ionization and slowing down calculations. We take the initial NBI ionization profile from PENCIL [41] while the beam slowing down calculation and the ripple effect is accounted for with ASCOT.

Figure 8 summarizes the result of torque evaluation for the three discharges. It shows the time traces of the volume integrated torque components and the time averaged torque

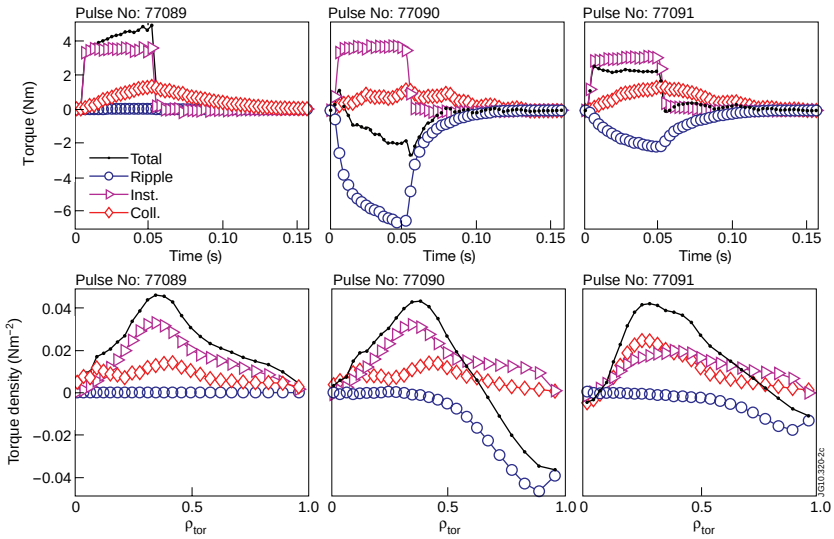

Figure 8. One modulation cycle data for the modulated NBI units only. Top row shows the volume integrated torque separated in ripple, collisional and instantaneous components. Bottom row shows cycle averaged torque densities for each component. 77089 is the reference case with normal NBI, 77090 is with normal NBI and ripple, and 77091 is with tangential NBI and ripple. Note that 77091 uses only two modulated NBI units.

densities for the modulated NBI units only. For better illustration only one NBI modulation cycle is pictured. The total torque is split into three components each with distinct time scale: *collisional* torque due to Coulomb collisions, *instantaneous* torque which is essentially the toroidal component of the $\boldsymbol{j} \times \boldsymbol{B}$ force arising from the difference in the initial and bounce averaged flux surface of the ions. Third, the *ripple* torque is due to the non-ambipolar radial diffusion of the NBI ions in the non-axisymmetric magnetic field. They all have different time scales and must be correctly resolved for simulating the inherently time-dependent NBI modulation experiments.

As shown in figure 8, collisional torque is the slowest of the torque transfer mechanisms and it takes place in fast ion slowing down time ($\sim$150 ms). Instantaneous torque, as the name suggests, is transferred immediately relative to the usual slowing down time. Even in the absence of collisions it will take place in about one bounce time ($\sim$50 μs) during which the initial bounce phases of the injected ions are randomized. Note that due to technical reasons in all the plots in this section, the instantaneous torque includes a small and delayed $\boldsymbol{j} \times \boldsymbol{B}$ torque component, which arises when collisions (or ripple) transform passing ions into trapped ones or vice versa. It is relatively easy to see that the time scale for the ripple torque must be somewhere between the $\boldsymbol{j} \times \boldsymbol{B}$ and collisional torques. This is because ripple diffusion only occurs at the tips of the trapped ion banana orbits, and it necessarily takes several bounce times before any significant effect is accumulated. On the other hand, ripple diffusion scales with the fast ion energy (see equation (1)), making the effect faster than the fast ion slowing down time. The simulations indeed confirm the dynamics.

It is, furthermore, interesting to note that in the case of normal NBI modulation, the generated ripple torque exceeds co-current torque components and therefore makes the total

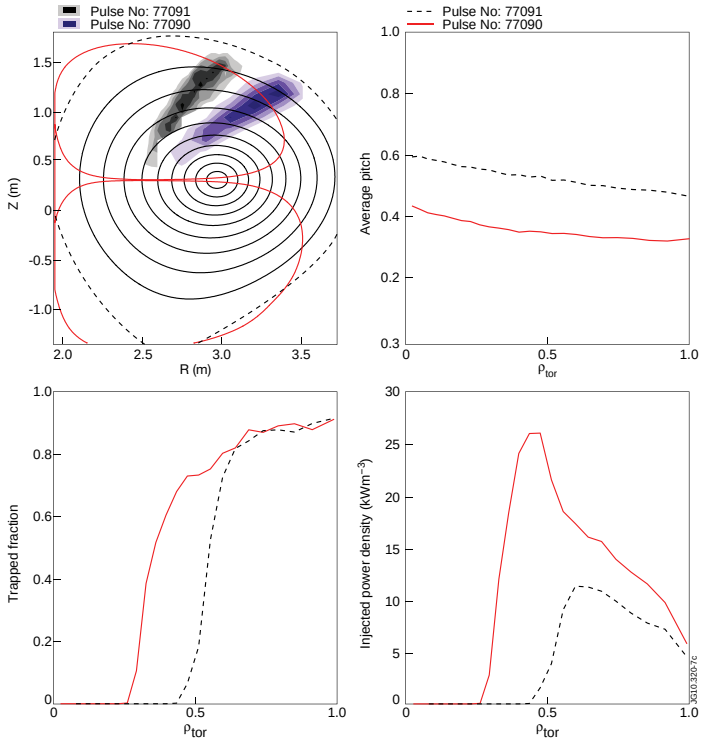

Figure 9. Initial NBI characteristics for trapped ions. (*a*) Turning point density on poloidal cross section for normal (77090) and tangential (77091) injection. The red lines confine a ripple well free region. (*b*) The average initial pitch of all NBI ions, (*c*) the fraction of trapped ions and (*d*) the injected energy density of trapped ions.

modulated torque near the edge negative. Also with the tangential injection, the total deposited torque near the edge becomes counter-current, however, at much smaller margin.

The main differences in the ripple torque generation between the normal and tangential injections can be qualitatively understood from figure 9. The plot on the top left frame shows the initial turning point density and the ripple trapping boundary for the normal (77090) and the tangential (77091) injection. This can be compared with figure 4 to see that with the normal injection the initial turning points locate in a region where the ripple is higher. The average pitch, $\xi = v_{||}/v$, of the newly ionized ions as a function of minor radius is shown on the top right frame. In absolute numbers, the difference between the normal and the tangential injection does not appear to be large, but since the pitch angle scattering becomes more effective at lower energies, the ions from the tangential injection have transferred much of their energy and momentum to the plasma before their average pitch equals that of the normal injection.

The fractions of initially trapped ions are shown in the bottom left frame. While there is a significant difference inside the midradius, the fractions are nearly the same where the ripple is highest, i.e. near the edge. The bottom right figure shows the injected power density of initially

trapped ions. Due to the one less modulated injector, the power density is roughly 30% smaller in the tangential case. This is much too small to account for the factor of 3 difference in the ripple torque between the normal and tangential injection (see figure 8). Also, while not instantly apparent from the figure, the rise time of the generated ripple torque is significantly shorter for the normal injection than it is for the tangential injection. The explanation for these differences can be attributed to the turning point locations. In normal injection, the turning points are instantaneously close to the maximum ripple level of a given flux surface, unlike the ions from the tangential injection. A significant fraction of fast ion slowing down time is spent before the pitch angle scattering has diffused the turning points from tangential NBI into the stronger ripple region. This will both add delay, and reduce the magnitude of the ripple torque in the case of tangential NBI. More details of the torque profiles are shown in the next section, where they are Fourier transformed and plotted side-by-side with the corresponding experimental rotation profiles.

4.2. Rotation measurements

The toroidal rotation of the plasma is measured with a charge exchange recombination spectroscopy (CXRS) diagnostic based on carbon emission lines. The diagnostic has 12 horizontal lines of sight into the plasma which, in this configuration, cover the radius from the centre to the pedestal top, with a time resolution of 10 ms, and $\pm 5\%$ measurement error [42]. Based on earlier experiments on JET [43], and the weak temperature gradients in these discharges, we expect that the bulk plasma (deuterium) rotation is nearly identical to that of the carbon.

Figure 10 shows the toroidal angular frequency of the 3 discharges, as a function of time, for three modulation cycles within the analysis window. The grey areas in the figures indicate the times the modulated NBI is switched on. From this data one can see the spin-up of the plasma when NBI is turned on. However, for discharge 77090 with ripple, near the separatrix (lines at the bottom) the plasma actually accelerates in the opposite direction indicating that, near the edge, the ripple torque exceeds the co-current momentum from the NBI.

For a more quantitative analysis of the experimental rotation profiles we Fourier transform the data for all radial locations. The result at the 6.25 Hz NBI modulation frequency is shown in figure 11 (left column), where the rotation amplitudes, phases and the steady-state profiles are plotted for the three discharges. For comparison the corresponding source terms from ASCOT, i.e. toroidal torque amplitude, phase and steady state, are plotted adjacent on the right column. The similarity of the experimental rotation amplitude and phase profiles and the correspondent calculated torque amplitude and phase profiles is striking. The calculation of the torque is completely independent of the rotation profile, so this clearly indicates the strong influence of the NBI torque on the toroidal rotation. Even before the momentum transport analysis, the topic in the next section, one can see that the rotation profiles and their shapes seem to be consistent with the source profiles.

One of the most obvious differences between the discharges is the higher steady-state rotation of the reference discharge, see bottom left frame of figure 11. It gives a clear indication of the existence of a large counter-current torque in the rippled discharges. In section 4.1 it was found that ions from normal NBI experience stronger ripple effect than those from the tangential NBI. This is also clearly visible in the amplitude and phase plots for both the rotation and torque where the normal NBI with ripple (77090) has larger and deeper penetrating amplitude than the one for the tangential NBI (77091). Note that the injected torque from three normal NBI units is $\sim$15% larger than the torque from two tangential units. The stronger ripple effect on normal NBI is also evident in the steady-state profiles for rotation and torque. It is interesting

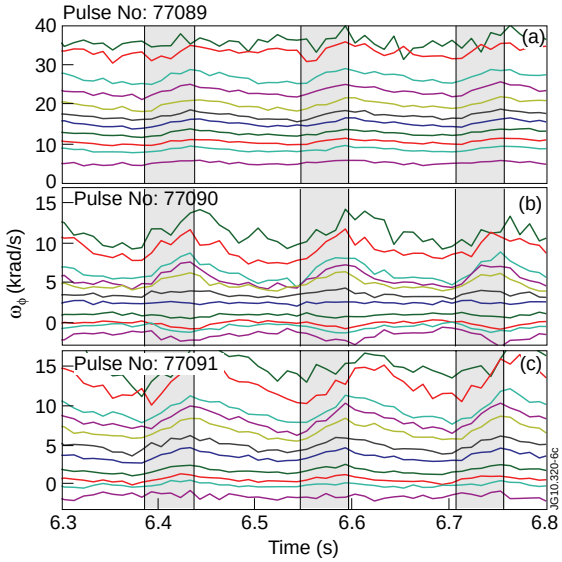

Figure 10. Time traces of CX measurements of toroidal angular frequency at various lines of sight for (*a*) normal NBI without ripple (77089), (*b*) normal NBI with ripple (77090) and (*c*) tangential NBI with ripple (77091). Grey bars indicate the time when modulated NBI is on. Due to the monotonic rotation profile (see figure 3) high values correspond to the centre ($R = 3.05$ m) and low values to the edge of the plasma ($R = 3.78$ m).

to note that the radius of the minimum amplitude for the rotation and the torque for the normal NBI with ripple (77090) coincide at $\rho_{\mathrm{tor}} = 0.6$. This is, in fact, an important feature since it was found to improve the robustness of the torque validation by making the analysis less sensitive to the details of the toroidal momentum transport. Finally, it may first seem odd that inside the midradius, where the ripple amplitude is negligible and where the torque profiles are identical for the normal NBI cases with (77090) and without (77089) ripple, that there is a difference in the rotation phases. This feature, however, is well reproduced in the momentum transport analysis when both the pinch and the diffusion terms are included.

5. Ripple torque validation

As already mentioned, no diagnostic exists that can measure the injected torque directly. CXRS diagnostics can measure the carbon rotation but momentum transport analysis are required to relate the calculated torque source with the rotation. In our transport analysis we assume that for the torque source the reference discharge is calculated accurately with ASCOT, allowing us to use the NBI modulation technique to determine the momentum transport coefficients (Pr, v_{pinch}) without resorting to theoretical models or assumptions other than the momentum transport being independent of the NBI power modulation.

In this work we build on the scheme used in an earlier work [6, 32, 33, 44, 45] to find the optimal profiles for the Prandtl number and the pinch velocity. Here we replace the manual trial and error profile optimization with a non-linear minimizing routine that allows simultaneous

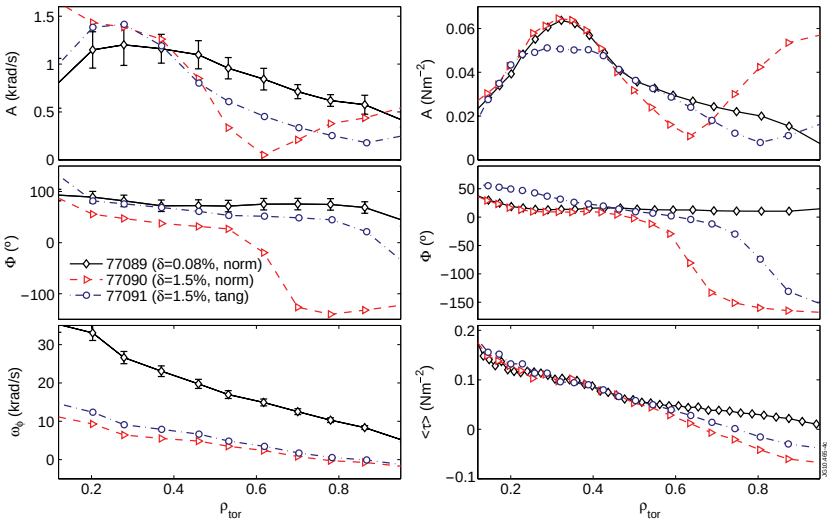

Figure 11. Fourier amplitudes (top), phases (middle) and steady-state values (bottom) of the experimental toroidal rotation profiles (left column) and calculated torque profiles (right column).

fitting of both pinch velocity and Prandtl number profiles. We also make an effort to set suitable optimization criteria *a priori* and let the minimization routine to find the Pr and v_{pinch} profiles that best reproduce the measured rotation profile in an automated way. Note that at this stage we only use data from the reference case since the torque calculations without ripple are already validated. Later we use these results to benchmark the ripple torque calculations.

Similar to the previous work, we use JETTO transport code to calculate the plasma response to the injected torque for the given Pr and v_{pinch} profiles. We take the resulting time-dependent rotation profile and Fourier transform it on all radii to obtain rotation amplitude and phase profiles at the NBI modulation frequency, and to get the steady-state profile. The minimization routine varies the Pr and v_{pinch} profiles until they produce the best possible match between the simulated rotation response and the experimental data for the amplitude, phase and steady-state profiles simultaneously. As a figure of merit for the error in each profile we use the mean squared error against the experimental data which we normalize so that the error for the amplitude, phase and the steady state all yield roughly the same value near the optimum. The individual normalized errors are added together and the resulting error is the target of the minimization.

Typically in one optimization, with 5 radial points each for pinch and Prandtl number profiles, hundreds of transport simulations are needed for converged solution. To ensure the robustness in finding the global optimum in the multi-dimensional parameter space, we launch the above optimization cycle several times, each with a randomly selected initial Pr and v_{pinch} profiles. In this procedure, we usually find that most of the optimized profiles converge to the same solution giving the assurance that the global optimum is found. During the optimization the torque source is taken from ASCOT calculation.

In figure 12 the result of the above optimization cycle is shown for 77089. Black squares are the experimental data and the ensembles of red lines show the amplitude, phase and

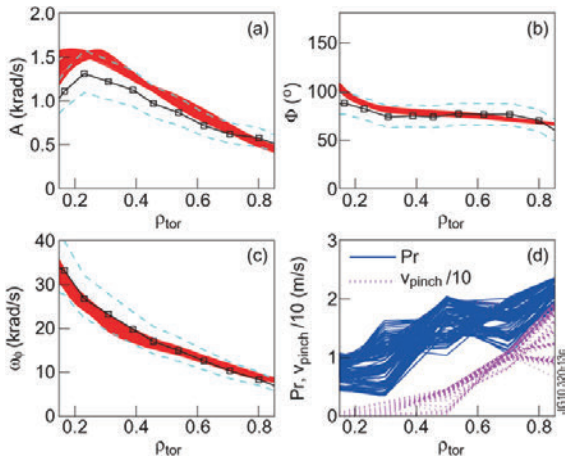

Figure 12. The ensemble of red lines give the rotation (*a*) amplitude (*b*) phase (*c*) steady state of the simulations that yield a target error that is within 10% of the best fit. The corresponding Prandtl number and pinch velocity profiles are plotted in the lower right frame. Black lines with square markers show the experimental data and the dashed lines give the 20% interval around the measurements for rotation and rotation amplitude and 11.25° (5 ms equivalent in time) for phase and help to quantify the quality of the fit.

steady-state profiles from all converged and nearly converged states where the total error is within 10% of the best fit. The dashed lines in the amplitude and steady-state plots show the ±20% variation and are there to help quantify the level of agreement achieved. The dashed line in the phase plot shows the ±11.25° variation corresponding to a 5 ms time resolution. In the simulations we use 3–5 ms resolution for the data, while the time integration period for the rotation measurement is 10 ms, thus making the 5 ms as a reasonable estimate for the phase error. The bottom right frame in figure 12 shows the set of the pinch velocity and Prandtl number profiles that correspond to the described amplitude, phase and steady-state profiles.

We find that roughly 30% variation in transport coefficients around the optimum is allowed while still giving a good fit against the experiment. There are a few reasons why this can be expected. Firstly, small changes in the diffusion coefficient can, to some extent, be compensated by appropriate changes in the pinch velocity without increasing the total error significantly. Secondly, the definition of the total error (mean squared error) is not very sensitive to the profile shapes and can yield similar errors for qualitatively different profiles. Furthermore, as typical for profile optimization, a small change in one profile point can partly be compensated by changes in the neighbouring points. However, even with the scatter in the profiles one can easily recognize the increasing trend towards the edge in both profiles which is consistent with the earlier work [6, 11].

The optimal profiles for the Prandtl number and the pinch velocity are shown in figure 13. We find that, apart from the centre of the plasma, the Prandtl number stays above unity in these L-mode discharges, while slightly smaller values were previously found for the H-mode discharges [33] and in theory [46]. It is noteworthy also that, for the first time on JET L-mode plasmas, we find that a non-zero pinch velocity is required to fit the rotation amplitude, phase and steady-state profiles simultaneously.

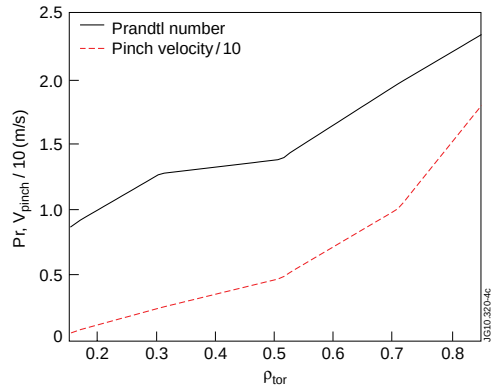

Figure 13. Optimized Prandtl number and pinch velocity profiles for 77089.

The main piece of evidence in the experimental ASCOT NBI torque validation effort is shown in figure 14 where the comparison between the simulated toroidal rotation and the experimental measurements are plotted for each discharge. Note that the momentum transport is assumed to be the same across all discharges as discussed earlier. It is seen that the simulated rotation response to the NBI modulation agrees well with the measurements. For all cases, the time response (phase) is matched within about 11.25° corresponding to about 5 ms time resolution. Also the amplitude and steady-state rotation profiles agree with the experimental data to within 20%. Furthermore, during the analysis it was seen that for the normal injection with ripple (77090) the radius where the phase of simulated rotation changes its sign, $\rho_{\mathrm{tor}} = 0.6$, is almost entirely determined by the torque source profile. Using Prandtl numbers that were smaller than the optimal found made the gradient too steep and, conversely, Prandtl numbers larger than the optimum flattened the gradient. However, the radius where the sign reversal occurs remained largely unaffected. These observations suggest that the NBI torque profiles with large ripple are consistent with measurements, a conclusion which is not very sensitive to the details of the momentum transport.

For completeness we used the optimization scheme also for the discharges with ripple to see if the optimized transport would differ from the one obtained from the reference case (see figure 13). We found that the agreement between the simulated and the measured rotation amplitude, phase and steady-state profiles were only marginally improved compared with using the transport from the reference discharge. This also implies that the momentum transport is indeed similar among the 3 discharges.

6. Conclusions

We have shown for the first time an experimental validation of a NBI torque profile calculation in the presence of large magnetic field ripple. We have used NBI modulation technique to deduce the prevalent momentum transport, and time-dependent torque calculations from ASCOT to make the comparison. We have developed a semi-automated way to analyse the transport in the NBI modulation experiments, based on a least squares optimization scheme, to obtain a more comprehensive picture of the transport sensitivity. We have also validated ASCOT ripple operation numerically against OFMC by comparing the heat load from ripple trapped ions, and

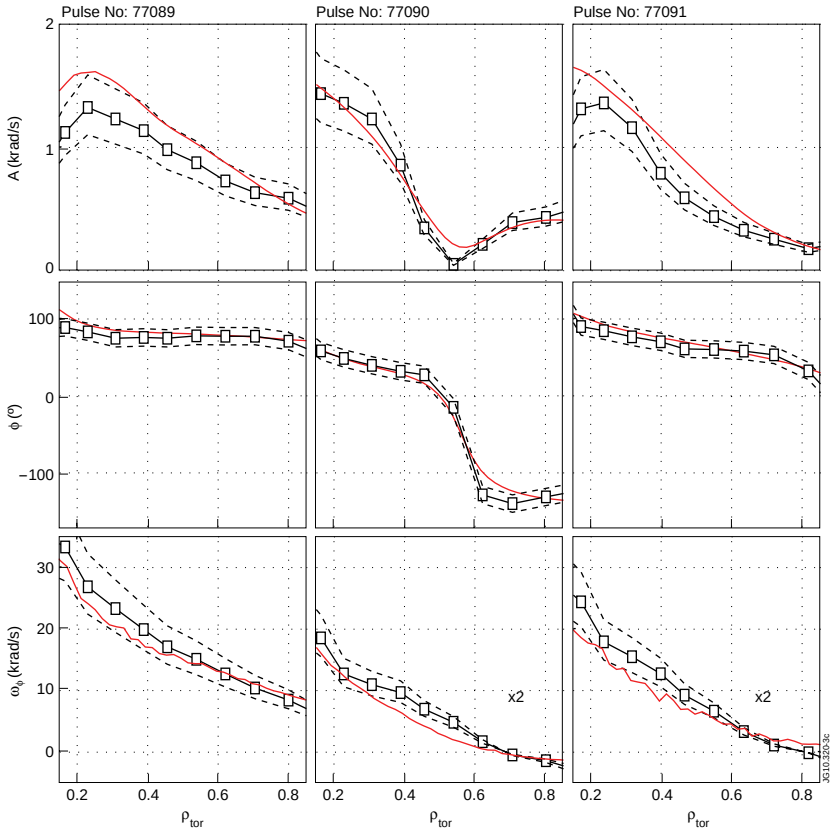

Figure 14. Amplitude, phase and steady-state profiles for the three discharges using the optimized Prandtl number and pinch velocity profiles for 77089 (see figure 13). The first column corresponds to the 77089, the second column to 77090 and the third column to 77091. Dashed lines are a guide to the eye and give rough estimates of the error.

showed good agreement against TRANSP for the time-dependent NBI torque evaluation without ripple. Although only JET L-mode discharges, optimized for the ripple torque validation, were used in this work, the previous work with heat load and torque validation, e.g. [19, 24], suggests that the guiding centre following Monte Carlo approach is accurate more generally and can be used for predicting the NBI torque under conditions where the guiding centre approximation holds.

In this work we only considered NBI for the core torque source. The modulated torque especially should be clearly dominated by the NBI and ripple, since the small induced plasma perturbations ($\delta T_e, \delta T_i, \delta q, \delta n_e$) due to the NBI are not expected to modify the turbulent character of the plasma significantly. However, it is possible that some intrinsic sources were contributing to the steady-state torque. While they are mainly expected to be edge localized [46], experimental evidence for intrinsic core sources have also been reported [47].

During the transport analysis we did observe, similar to some earlier H-mode cases [6, 33], that for the best overall fit (simultaneous fit of the amplitude, phase and steady-state rotation) the simulated rotation amplitudes tended to get slightly overestimated and the steady-state rotation underestimated. While, on the one hand, this could indicate a small error in the NBI torque calculations, it may also point to an intrinsic core torque contribution like residual stress in the co-current direction. It must be noted, however, that because of the good agreement shown here, the intrinsic core torque source in these discharges should be small.

For future work this method will be modified to allow systematic estimation of the magnitude of the intrinsic torque source in the core plasma even in the presence of NBI torque. For edge localized torque source studies this scheme would seem not to be as promising due to less accurate measurements in the pedestal region which makes it more difficult to separate the sources from the boundary contribution.

Acknowledgments

The authors wish to thank Dr N Oyama and Dr K Shinohara for their help in setting up OFMC for JET and Dr D Howell for providing the vacuum ripple map.

This work, supported by the European Communities under the contract of Association between EURATOM and Tekes, was carried out within the framework of the European Fusion Development. The views and opinions expressed herein do not necessarily reflect those of the European Commission.

References

[1] Biglari H, Diamond P H and Terry P W 1990 Influence of sheared poloidal rotation on edge turbulence *Phys. Fluids B: Plasma Phys.* **2** 1–4

[2] Garofalo A M *et al* and DIII-D Team 2001 Resistive wall mode dynamics and active feedback control in DIII-D *Nucl. Fusion* **41** 1171

[3] Peeters A G, Angioni C and Strintzi D 2007 Toroidal momentum pinch velocity due to the Coriolis drift effect on small scale instabilities in a toroidal plasma *Phys. Rev. Lett.* **98** 265003

[4] Hahm T S, Diamond P H, Gurcan O D and Rewoldt G 2007 Nonlinear gyrokinetic theory of toroidal momentum pinch *Phys. Plasmas* **14** 072302

[5] Yoshida M, Koide Y, Takenaga H, Urano H, Oyama N, Kamiya K, Sakamoto Y, Matsunaga G, Kamada Y and the JT-60 Team 2007 Momentum transport and plasma rotation profile in toroidal direction in JT-60U L-mode plasmas *Nucl. Fusion* **47** 856

[6] Tala T *et al* 2009 Evidence of inward toroidal momentum convection in the JET tokamak *Phys. Rev. Lett.* **102** 075001

[7] Solomon W M *et al* and the DIII-D Rotation Physics Task Force 2009 Advances in understanding the generation and evolution of the toroidal rotation profile on DIII-D *Nucl. Fusion* **49** 085005

[8] de Vries P C, Versloot T W, Salmi A, Hua M-D, Howell D H, Giroud C, Parail V, Saibene G, Tala T and JET EFDA Contributors 2010 Momentum transport studies in JET H-mode discharges with an enhanced toroidal field ripple *Plasma Phys. Control. Fusion* **52** 065004

[9] Tala T *et al* 2010 JET rotation experiments towards the capability to predict the toroidal rotation profile *Proc. 23rd Int. Conf. on Fusion Energy, (Daejeon, Korea, 2010)* EXC/3-1

[10] Shinohara K, Oikawa T, Urano H, Oyama N, Lönnroth J, Saibene G, Parail V and Kamada Y 2009 Effects of ferromagnetic components on energetic ion confinement in ITER *Fusion Eng. Des.* **84** 24–32

[11] de Vries P C *et al* and JET EFDA Contributors 2008 Effect of toroidal field ripple on plasma rotation in JET *Nucl. Fusion* **48** 035007

[12] Nave M F F, Johnson T, Eriksson L-G, Crombé K, Giroud C, Mayoral M-L, Ongena J, Salmi A, Tala T and Tsalas M 2010 Influence of magnetic field ripple on the intrinsic rotation of tokamak plasmas *Phys. Rev. Lett.* **105** 105005

[13] Callen J D 2010 Effects of 3D magnetic perturbations on toroidal plasmas *Proc. 23rd Int. Conf. on Fusion Energy (Daejeon, Korea, 2010)* OV/4-3
[14] Diamond P H, McDevitt C J, Gürcan Ö D, Hahm T S, Wang W X, Yoon E S, Holod I, Lin Z, Naulin V and Singh R 2009 Physics of non-diffusive turbulent transport of momentum and the origins of spontaneous rotation in tokamaks. *Nucl. Fusion* **49** 045002
[15] Goldston R J, White R B and Boozer A H 1981 Confinement of high-energy trapped particles in tokamaks *Phys. Rev. Lett.* **47** 647–9
[16] Yushmanov P N 1990 *Rev. Plasma Phys.* **16** 117
[17] Heidbrink W W and Sadler G J 1994 The behaviour of fast ions in tokamak experiments *Nucl. Fusion* **34** 535
[18] Boivin R L, Zweben S J and White R B 1993 Study of stochastic toroidal field ripple losses of charged fusion products at the midplane of TFTR *Nucl. Fusion* **33** 449
[19] Shinohara K *et al*, the JFT-2M Group and Darrow D S 2003 Effects of complex magnetic ripple on fast ions in JFT-2M ferritic insert experiments *Nucl. Fusion* **43** 586
[20] Tobita K, Tani K, Neyatani Y, van Blokland A A E, Miura S, Fujita T, Takeuchi H, Nishitani T, Matsuoka M and Takechi S 1992 Ripple-trapped loss of neutral-beam-injected fast ions in JT-60U *Phys. Rev. Lett.* **69** 3060–3
[21] Ikeda Y, Tobita K, Hamamatsu K, Ushigusa K, Naito O and Kimura H 1996 Ripple enhanced banana drift loss at the outboard wall during ICRF/NBI heating in JT-60U *Nucl. Fusion* **36** 759
[22] Heidbrink W W, Kim J and Groebner R J 1988 Comparison of experimental and theoretical fast ion slowing-down times in DIII-D *Nucl. Fusion* **28** 1897
[23] Ruskov E, Heidbrink W W and Budny R V 1995 Diffusion of beam ions at the tokamak fusion test reactor *Nucl. Fusion* **35** 1099
[24] deGrassie J S, Groebner R J and Burrell K H 2006 Prompt toroidal momentum balance with collisionless neutral beam injected torque in DIII-D *Phys. Plasmas* **13** 112507
[25] de Vries P C *et al* and JET EFDA Contributors 2008 Effect of toroidal field ripple on the formation of internal transport barriers *Plasma Phys. Control. Fusion* **50** 065008
[26] Heikkinen J A and Sipilä S K 1995 Power transfer and current generation of fast ions with large-k_θ waves in tokamak plasmas *Phys. Plasmas* **2** 3724–33
[27] Heikkinen J A, Herrmann W and Kurki-Suonio T K 1998 Fast response in the ripple trapped ion distribution to abrupt changes in a radial electric field in tokamaks *Nucl. Fusion* **38** 419
[28] Salmi A, Johnson T, Parail V, Heikkinen J, Hynönen V, Kiviniemi T P, Kurki-Suonio T and JET EFDA Contributors 2008 Ascot modelling of ripple effects on toroidal torque *Contrib. Plasma Phys.* **48** 77–81
[29] Tani K, Azumi M, Kishimoto H and Tamura S 1981 Effect of toroidal field ripple on fast ion behavior in a tokamak *J. Phys. Soc. Japan* **50** 1726–37
[30] Pankin A, McCune D, Andre R, Bateman G and Kritz A 2004 The tokamak Monte Carlo fast ion module nubeam in the national transport code collaboration library *Comput. Phys. Commun.* **159** 157–84
[31] Duesing G, Altmann H, Falter H, Goede A, Haange R, Hemsworth R S, Kupschus P, Stork D and Thompson E 1987 Neutral beam injection system *Fusion Technol.* **11** 163–202 (cited By (since 1996) 44)
[32] Tala T *et al* and JET-EFDA Contributors 2007 Toroidal and poloidal momentum transport studies in tokamaks *Plasma Phys. Control. Fusion* **49** B291
[33] Mantica P *et al* and JET-EFDA Contributors 2010 Perturbative studies of toroidal momentum transport using neutral beam injection modulation in the joint european torus: Experimental results, analysis methodology, and first principles modeling *Phys. Plasmas* **17** 092505
[34] Mattor N and Diamond P H 1988 Momentum and thermal transport in neutral-beam-heated tokamaks *Phys. Fluids* **31** 1180–9
[35] Lao L 1990 Efit *Nucl. Fusion* **30** 1035
[36] Goloborod'ko V Ya, Kolesnichenko Ya I and Yavorskij V A 1987 Alpha particle transport processes in tokamaks *Phys. Scr.* **T16** 46
[37] Suzuki Y, Nakamura Y and Kondo K 2003 Finite beta effects on the toroidal field ripple in three-dimensional tokamak equilibria *Nucl. Fusion* **43** 406
[38] Strumberger E, Günter S, Merkel P, Schwarz E and Tichmann C 2010 Self-consistent three-dimensional computations of non-axisymmetric ITER equilibria *Nucl. Fusion* **50** 025008
[39] Tobita K, Tani K, Nishitani T, Nagashima K and Kusama Y 1994 Fast ion losses due to toroidal field ripple in JT-60U *Nucl. Fusion* **34** 1097
[40] Johnson T *et al* and JET-EFDA contributors Halekar modelling of fast particle transport and losses with TF ripple in JET *10th IAEA Technical Meeting on Energetic Particles in Magnetic Confinement Systems (Kloster Seeon, Germany)*
[41] Challis C D *et al* 1989 *Nucl. Fusion* **29** 563

[42] Carine Giroud, Meigs A G, Negus C R, Zastrow K-D, Biewer T M, Versloot T W and JET-EFDA Contributors 2008 Impact of calibration technique on measurement accuracy for the JET core charge-exchange system *Rev. Sci. Instrum.* **79** 10F525

[43] Testa D, Giroud C, Fasoli A, Zastrow K-D and EFDA-JET Team 2002 On the measurement of toroidal rotation for the impurity and the main ion species on the Joint European Torus *Phys. Plasmas* **9** 243–50

[44] Mantica P *et al* 2009 Experimental study of the ion critical-gradient length and stiffness level and the impact of rotation in the JET tokamak *Phys. Rev. Lett.* **102** 175002

[45] Tardini G, Ferreira J, Mantica P, Peeters A G, Tala T, Zastrow K D, Brix M, Giroud C, Pereverzev G V and JET-EFDA contributors 2009 Angular momentum studies with NBI modulation in JET *Nucl. Fusion* **49** 085010

[46] Peeters A *et al* 2010 Toroidal momentum transport *Proc. 23rd Int. Conf. on Fusion Energy (Daejeon, Korea, 2010)* OV/5-4

[47] Solomon W M *et al* 2010 Mechanisms for generating toroidal rotation in tokamaks without external momentum input *Phys. Plasmas* **17** 056108